SUPPLEMENTARY INFORMATION

Supplementary Figures

Figure S1. **QD-IgE is predominantly monovalent.** A number of analyses were performed to assess the valency of QD-IgE. In addition to the degranulation and biotinylation assays described in the main text, we carried out EM experiments (see Supplementary Methods for more detail) as shown here. (**a**) Representative electron micrograph of QD-IgE + DNP-BSA-gold. Gold particles (5 nm) are marked with white circles. Scale bar represents 100 nm. (**b**) Graph showing the distribution of the number of DNP-BSA-gold probes within 60 nm of QD-IgE (n = 107). We reason that if QD-IgE were predominantly monovalent, then each complex would have a maximum of two available binding sites for DNP-BSA-gold (IgE valency for DNP = 2). In fact, we find that the majority of the QDs have only one gold particle nearby, further supporting the monovalent nature of QD-IgE.

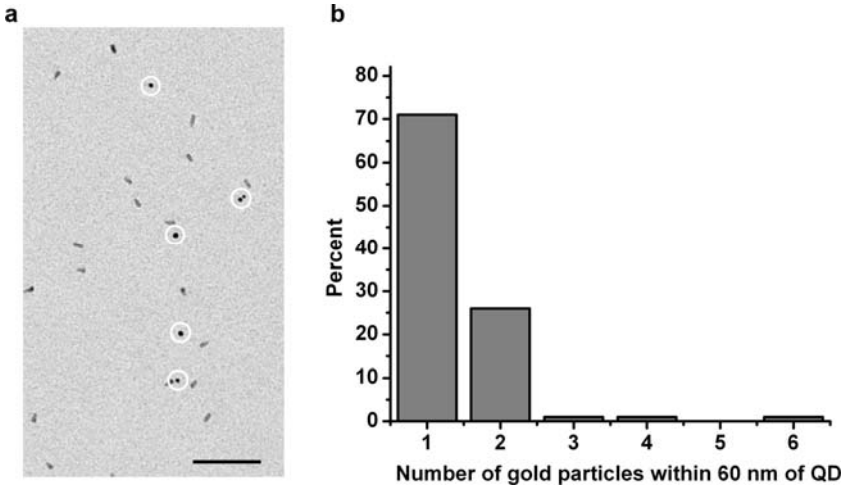

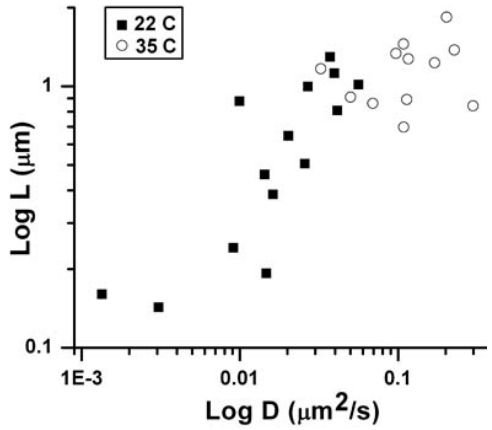

Figure S2. Influence of temperature on diffusion. Log-log plot of diffusion coefficient (D) versus restricted region size (L) for trajectories fitting the restricted diffusion model at 22°C (filled squares) and 35°C (open circles). The plotted D and L values were determined by fitting the restricted diffusion equation MSD = *offset* + $(L^2/3)(1-\exp(-\Delta t / \tau))$ (ref [1]), where $D=L^2/12\tau$ to the first 10% of the data points in each MSD plot. It is apparent that at physiological temperature, D is faster and L is larger than at ambient temperature.

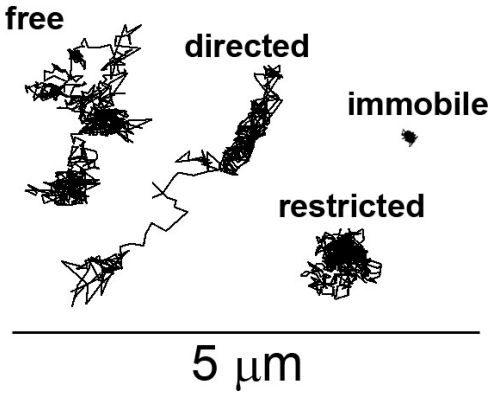

Figure S3. QD-IgE-FcεRI exhibits four motional modes. Representative trajectories of QD-IgE-FcεRI are shown. We observed four types of diffusion for FcεRI in resting cells at 35°C: free (65%), restricted (23%), immobile (4%) and directed (8%). Trajectories were classified by a slight modification of the method described in [2].

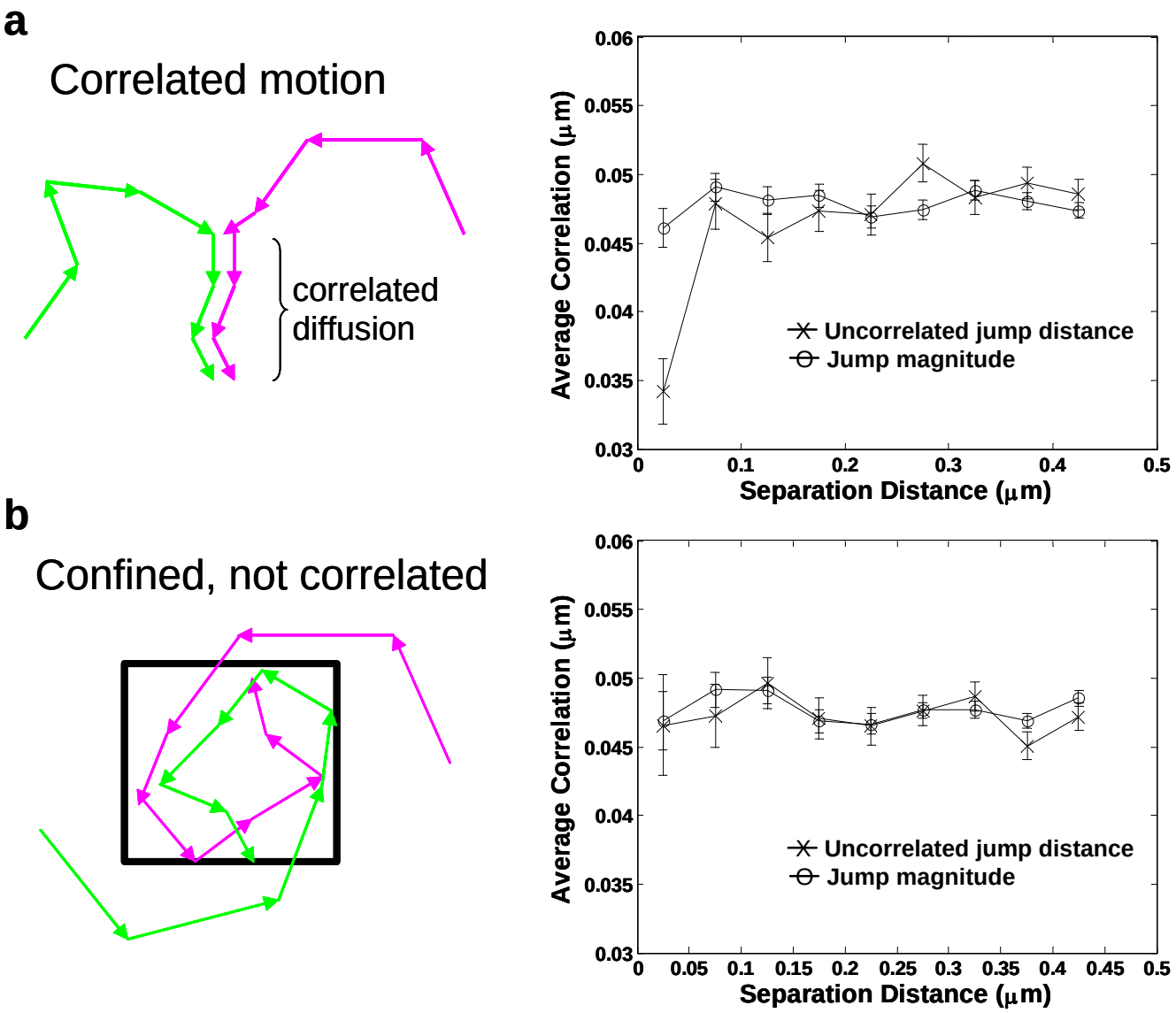

Figure S4. Analysis of simulated receptor dimerisation or co-confinement. Particles undergoing free Brownian diffusion (D = 0.07 $\mu m^2/s$) were tracked under dimerising (**a**) and non-dimerising (**b**) conditions. Parameters for the simulation included probability of binding (0.5), binding interaction distance (25 nm), localisation accuracy (15 nm) and QD blinking. (**a**) Left: Schematic showing the displacement vectors of two receptors that form a transient (up to 200 ms) dimer and undergo correlated motion. Right: Analysis of simulations of transient dimer formation. Note the pronounced decrease in the uncorrelated jump distance as diffusing particles approach each other to within the interaction distance. (**b**) Left: Schematic depicting the displacement vectors of two particles that maintain proximity due to confinement in a region (black square) but do not show correlated motion. Right: Analysis of simulations under the same conditions as **a**, except that the probability of binding was set to zero. Note that the uncorrelated jump distance does not vary significantly as a function of separation distance. Thus, even when these particles are close enough to show emission overlap, the analysis shows that their motion is not correlated. Given that the mechanism of decreased diffusion rate upon oligomerisation is poorly characterised in live cells, we did not attempt to include this phenomenon in our simulations and therefore the jump magnitude does not vary in these analyses.

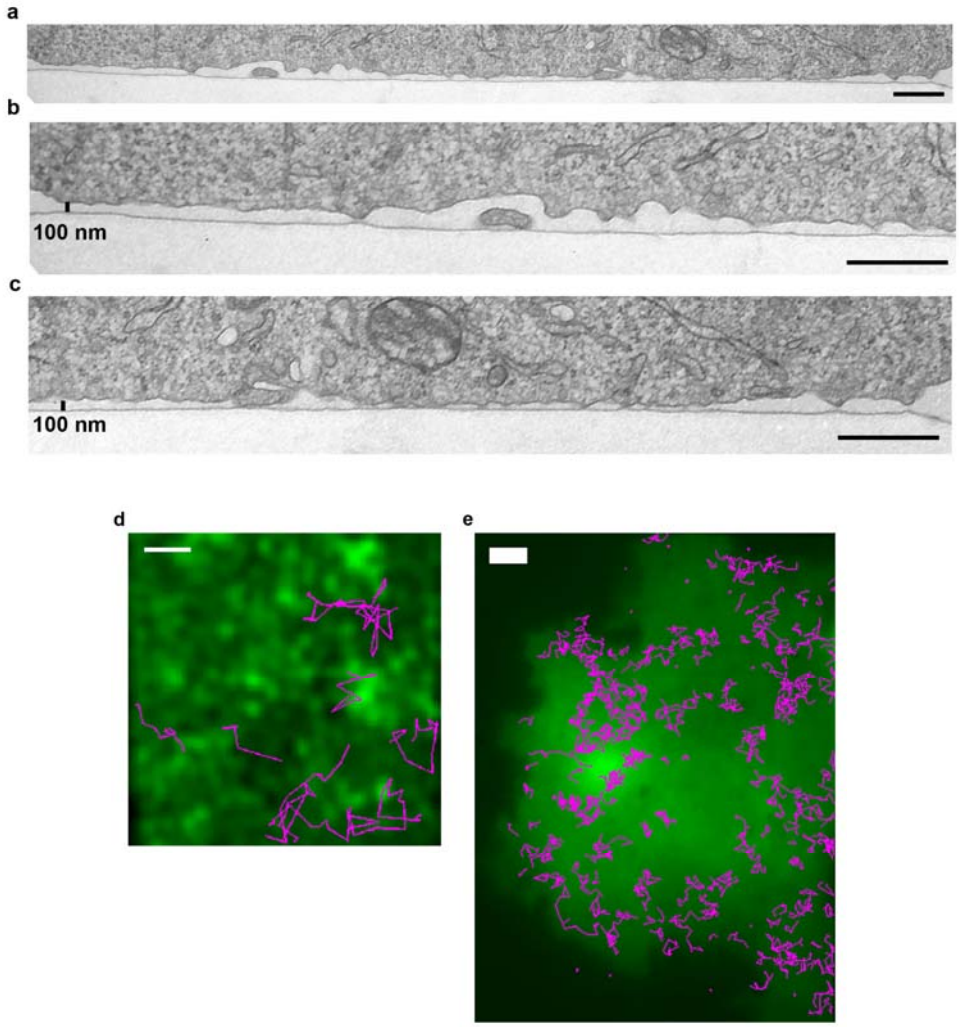

Figure S5. Membrane-coverslip distance does not dictate QD-IgE-FcεRI diffusion. (**a**-**c**) TEM image of an adherent RBL-2H3 cell taken perpendicular to the plane of adhesion (see Supplementary Methods). Images in **b** and **c** are the left and right half, respectively, of the region depicted in **a**. (**d**) TIRF image of GFP-actin (green) overlayed with trajectories of *free* QDs diffusing under the cell (magenta). (**e**) TIRF image of cytoplasmic GFP (green) overlayed with QD655-IgE-FcεRI trajectories (magenta) (see Supplementary Methods). Even regions closest to the coverslip (brightest GFP signal) do not exclude QD-IgE-FcεRI. Also note the highly disimilar patterns of GFP fluorescence in **d** and **e**; indicating that GFP-actin intensity does not correlate with membrane-coverslip distance as measured by cytoplasmic GFP intensity. (**f-q**) TIRF images of adherent, RBL-2H3 cells expressing GFP-actin (**f**, **g**, **j**, **k**, **n**, and **o**) or cytoplasmic GFP (**h**, **i**, **l**, **m**, **p**, and **q)** in the presence of a soluble, extracellular dye. First and third columns show images of GFP-actin (**f**, **j**, and **n**) and cytoplasmic GFP (**h**, **l**, and **p**) signal, respectively. Second and fourth columns (**g**, **i**, **k**, **m**, **o**, and **q**) show signal from a soluble fluorophore which diffuses underneath the cells and is brighter in regions where there is more space between the coverslip and cell membrane and dimmer in regions of close contact. Images are a mean of 50 time frames. A cell mask was generated from the GFP image and applied to **f-i** to remove the high background dye fluorescence surrounding the cell. Note that the large (~300kD) fluorophore has access to nearly all of the area underneath the cell. Selected GFP-actin structures (**f**, **j**, and **n**) or regions of cytoplasmic GFP intensity (**l-q**) are outlined in white and superimposed on both the GFP image and the image of the soluble fluorophore to facilitate comparisons between the two images. All images have been background subtracted. (**r**-**w**) Confocal images of fixed RBL-2H3 cells expressing GFP-actin enabling comparison of GFP-actin fluorescence (**r**, **u**, and green in **t** and **w**) with β3 or VLA4 (α4) integrin staining (**s**, **v**, and magenta in **t** and **w**) at the adherent surface. Confocal slice thickness is 1 μm. Images have been Gaussian filtered. Scale bars represent 1 μm in **a-d** and **r-w**, 2 μm in **e**, and **j-q** and 5 μm in **f-i**.

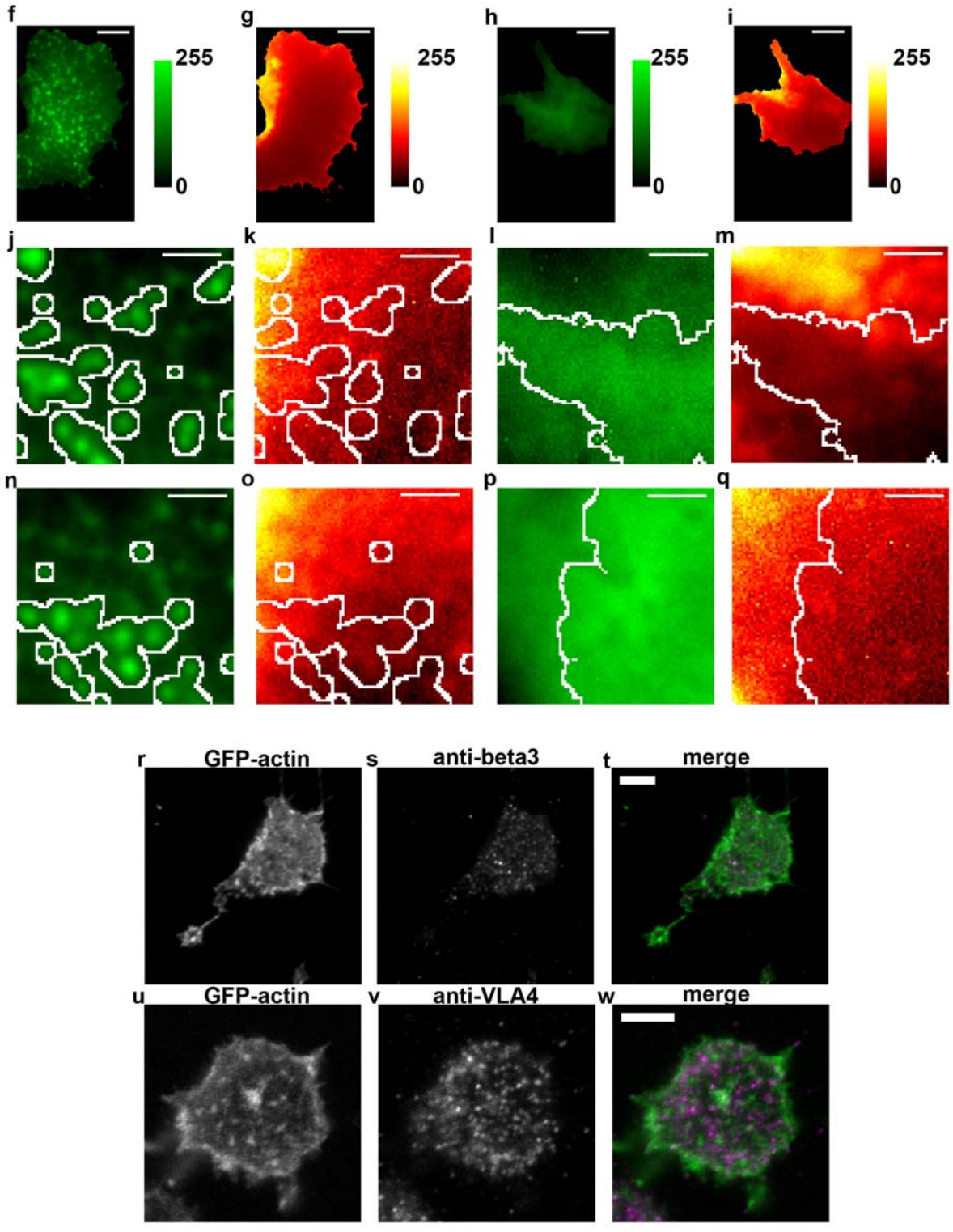

Figure S5 continued

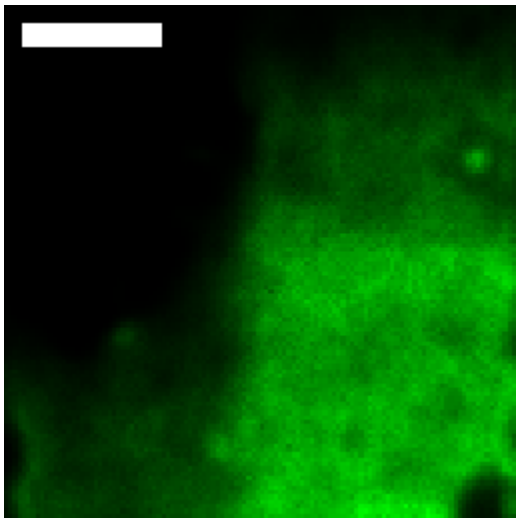

Figure S6. GFP-actin structure is visibly disrupted by latrunculin treatment. Deconvolved TIRF image of an RBL GFP-actin cell after 10 minute incubation with 500 nM latrunculin B. Note that less structure is apparent than in untreated cells (Figure S5a; Figure 4c in main text, and Supplementary Video 4). Scale bar represents 2 μm.

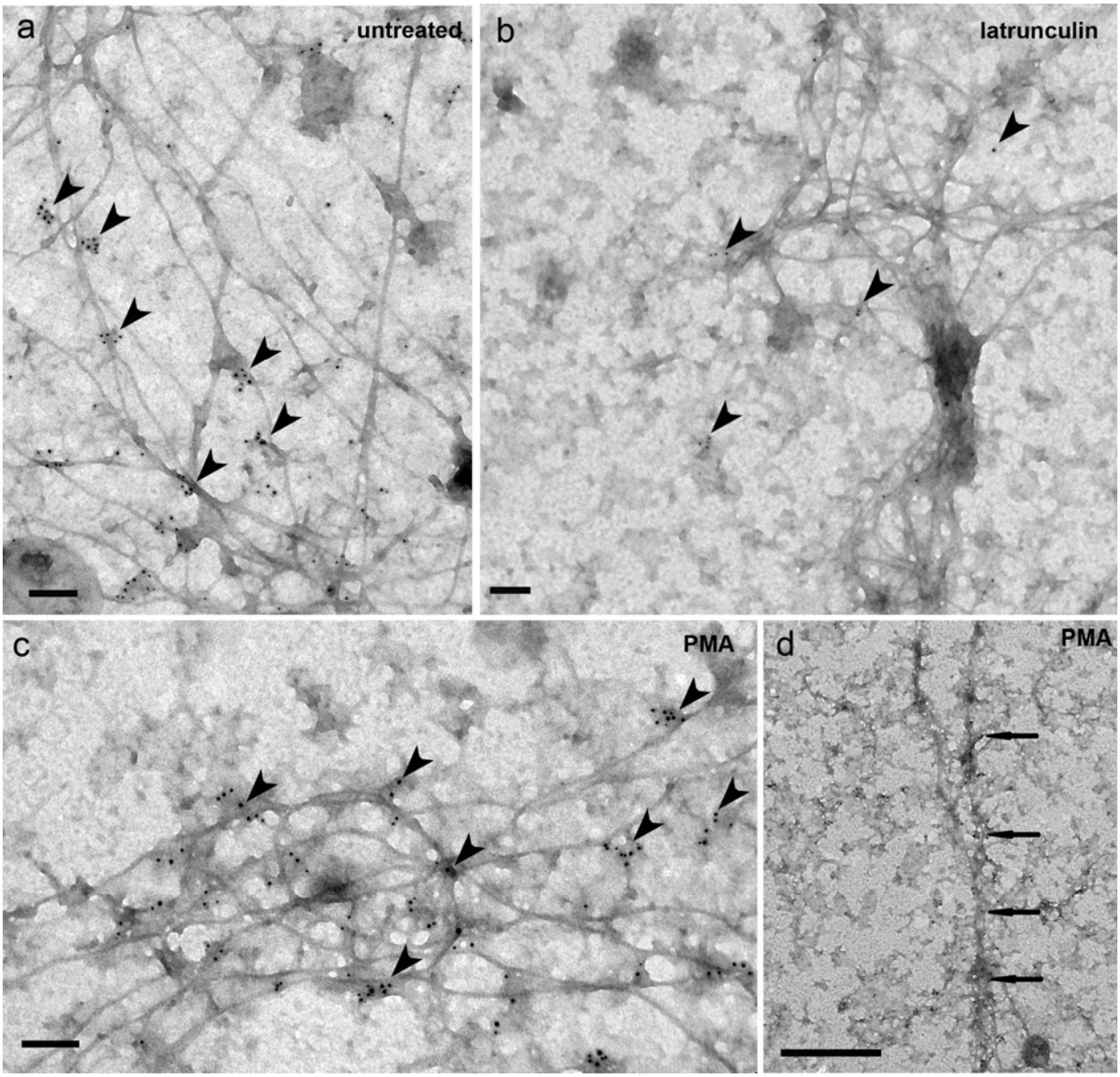

Figure S7. **Electron microscopy of membrane sheets**. Membrane sheets from the adherent surface of RBL cells (prepared as in reference 3 with the exception that cells were grown on EM grids) expressing GFP-actin. Gold particles label GFP-actin (arrowheads in **a-c**), which is located primarily at cytoskeletal junctions in the untreated (**a**) and PMA treated (50 nM for 30 min) (**c, d**) cells. This pattern is consistent with earlier observations[4]. Large actin bundles (arrows in **d**) likely correspond to GFP-actin structures visible by fluorescence micrsoscopy. After treatment with latrunculin B (10 μg/ml for 60 min), GFP labelling is dramatically decreased (indicating a disruption of the actin filaments), but cable-like structures are still present (presumably composed of an intermediate filament protein) (**b**). Scale bars represent 100 nm in **a-c** and 500 nm in **d**.

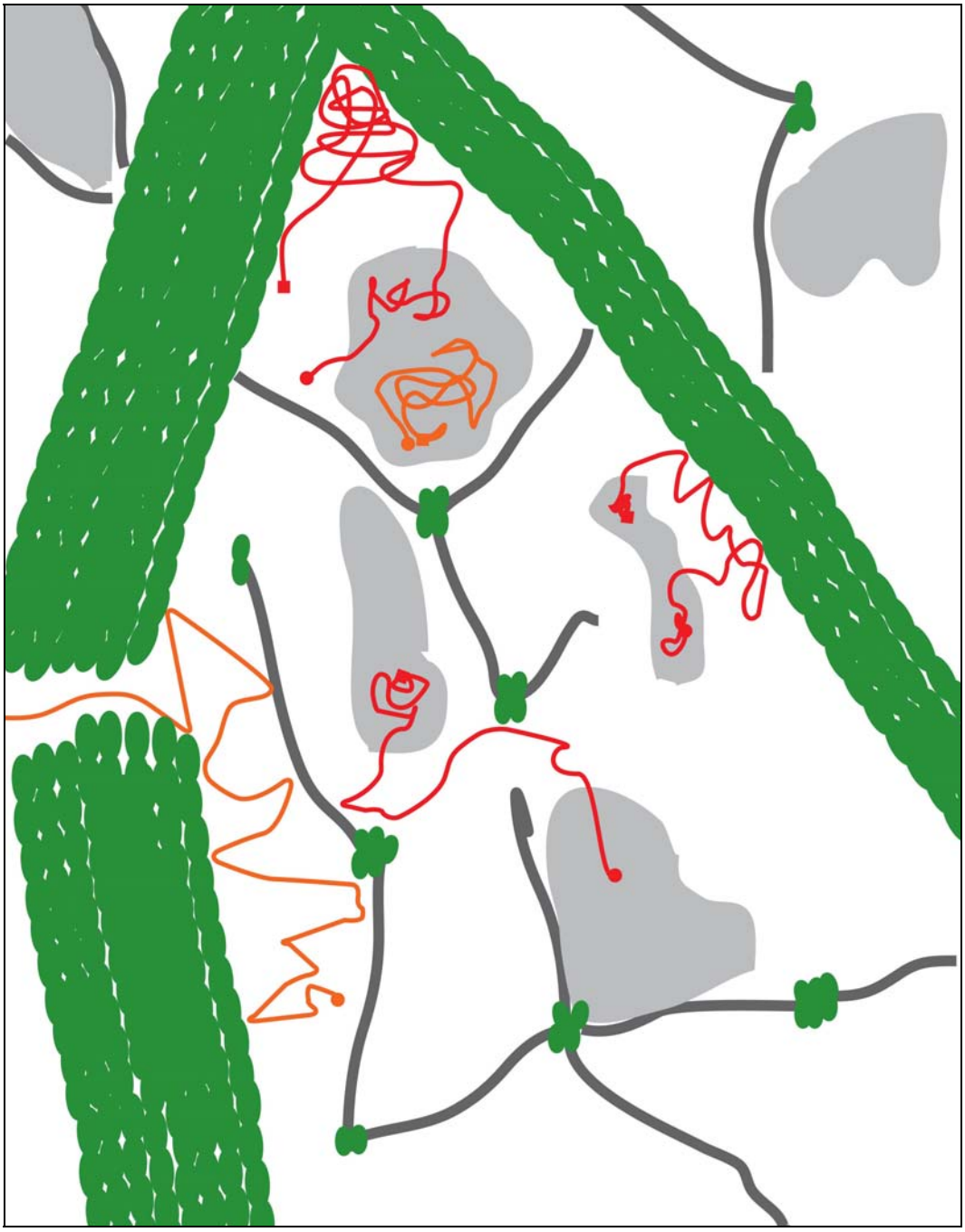

Figure S8. **Cartoon model of receptor movement through the membrane architecture**. Large actin bundles (green filaments), as observed in fluorescence microscopy, partition the membrane into large, micron-sized regions. Within this larger structure is a fine meshwork of cytoskeleton composed of intermediate filaments (dark grey) with actin at the junctions (as seen in EM) that form nano-scale domains. Additionally, membrane rafts (lipid rafts/protein islands, light grey) form specialised domains. Sample receptor trajectories (red, orange) are overlayed on this landscape, to demonstrate ways that these various components can restrict diffusion. Though a single snapshot of the membrane landscape is depicted here, in reality it is dynamically changing.

Supplementary Video Legends

Video 1 RBL-2H3 cell activation through QD-IgE. RBL-2H3 cell stably expressing FcεRIγ-mCFP (left panel), primed with 1 nM QD-IgE (middle panel) and stimulated with 14 nM DNP-BSA. Receptor aggregation and internalisation are readily apparent in the fluorescence channels, and cell ruffling and spreading can be seen in the DIC image (right panel). Images acquired at 37°C at 2 frames/min; playback is 5 frames/s. Fluorescence channels have been Gaussian filtered. Scale bar represents 10 μm.

Video 2 Co-confinement of multiple QD-IgE-FcεRI. RBL-2H3 cell labelled with 100pM QD655-IgE for 10 min at 37°C. Images acquired at 35°C at 33 frames/s, playback is 33 frames/s. Scale bar represents 5 μm.

Video 3 RBL-2H3 cells were transfected with GFP-actin, labelled with QD655-IgE and treated with PMA. Images of the two spectral channels were collected simultaneously on the same CCD camera at 33 frames/s and the two channels were made coincident by shifting the GFP-actin channel (green) using a Fourier based shift algorithm. SPT was performed on the QD-IgE images as described in the text. A small ~ 4x4 micron area centered on the region containing a QD-IgE trajectory was selected for further processing. The "green" channel containing the GFP-actin signal was de-noised and deconvolved as described. For improved visual clarity, the found positions of the tracked QD-IgE were used to generate a 2D Gaussian representation of the particle (magenta) and were combined as a colour overlay with the actin time series to generate a two-colour movie. Playback is 10 frames/s. Scale bar represents 1 micron.

Video 4 Restricted receptor diffusion on untreated RBL-GFP-actin cells. Same image processing details as in Video 3. Playback is 10 frames/s. Scale bar represents 1 micron.

Video 5 As described in the text, a 100 frame time series image was collected by imaging the top of the cell with a Zeiss 510 confocal microscope. RBL-2H3 cells were transected with GFP-actin (green) and labelled with QD-IgE (magenta) and were otherwise untreated. Emission was collected with a 545 nm dichroic mirror splitting emission to a 505 LP emission filter for GFP and the META detector was used as a bandpass filter (625-689 nm) to collect QD655 emission. Images were taken with 2× averaging, giving a final rate of 1 frame/s. Each frame of the GFP-actin image was de-noised using a wavelet based filter as described for the initial de-noise step in[5]. SPT was performed on the QD-IgE images as described in the text. For improved visual clarity, the found positions of the tracked QD-IgE were used to generate a 2D Gaussian representation of the particle (magenta) and were combined as a colour overlay with the actin time series to generate a two-colour movie. Playback is 10 frames/s. Scale bar represents 5 μm.

Supplementary Methods

EM analysis of QD-IgE valency

Solutions of 1nM QD-IgE or QD were prepared in PBS, 1% BSA and incubated on EM grids (formvar and carbon coated, then glow-discharged) for 15 min at room temperature. Grids were rinsed with PBS, then incubated with DNP-BSA-5nM gold (in PBS, 1% BSA) for 30 min at room temperature, followed by a PBS wash and fixation with 2% glutaraldehyde. Electron micrographs were acquired using a transmission electron microscope (Hitachi H600). From these images, we calculated averages of 1.3 and 6.5 DNP-BSA-gold particles per μm^2 for QD only (43.5 μm^2 total area) and QD-IgE (12.8 μm^2 total area) samples, respectively; indicating 20% non-specific binding of the DNP-BSA-gold probe. The average distances between each gold particle and the nearest QD were 92.7 and 51.4 nm for QD (n=57 gold particles) and QD-IgE (n=83 gold particles) samples, respectively.

TIRF controls

To ensure that interactions with the coverslip were not dictating QD-IgE-FcεRI motion, we performed several control experiments. We monitored diffusion of unbound streptavidin QD underneath GFP-actin cells (Fig. S6a), acquired cross-sectional EM images of adherent RBL-2H3 cells (Fig. S5), tracked QD-IgE-FcεRI complexes on the top (non-adherent) surface of RBL GFP-actin cells using confocal microscopy (Fig. 4 in main text) and on the bottom of RBL-GFP cells using TIRF microscopy (Fig. S6b), imaged RBL-GFPactin and RBL-GFP cells in the presence of soluble fluorophore (Fig. S7 and S8, respectively) using TIRF microscopy, and acquired confocal images of the adherent surface of fixed GFP-actin cells stained for the α4 and β3 integrins (Fig. S9). All of these experiments indicate that there is enough room for diffusion of the QD-IgE-FcεRI complex on the adherent cell surface and that the observed restriction of diffusion by actin structures is not merely a result of streic limitations due to membrane-coverslip proximity.

Free QD diffusion. SPT conditions were the same as for QD-IgE-FcεRI, except that unlabelled QDs that diffused between the cell and coverslip were tracked.

EM sections. Cells were grown as monolayers on plastic tissue culture dishes, and fixed with 2% glutaraldehyde in 0.1 M sodium cacodylate buffer. Cells were embedded in EPON and allowed to harden. The EPON-embedded cells were separated from the plastic surface and then mounted perpendicular to the plane of adhesion for sectioning. Sections were then processed and imaged as described previously[6].

RBL-GFP cells. RBL-GFP cells provided a means to visualise the topography of the adherent cell surface. Regions of the cell closer to the coverslip would have a larger volume within the TIRF field and therefore appear brighter, whereas regions further from the coverslip would have less volume within the TIRF field and appear dimmer. These cells were then labelled with 1 nM QD655-IgE and the QDs were tracked at 10 frames per second while simultaneously acquiring the cytoplasmic GFP signal.

Free dye. RBL-GFPactin or RBL-GFP cells were imaged at 5 frames/s in the presence of 20 nM Alexa Fluor® 647-R-phycoerythrin streptavidin (Invitrogen, Carlsbad, CA) in the imaging buffer. Regions of close contact between the cell and the coverslip exclude more of the soluble fluorophore and therefore have less fluorescence compared to regions which were further from the coverslip. By simultaneously acquiring the GFP-actin signal and the soluble fluorophore signal, we could compare the distribution of GFP-actin with the distance between the membrane and the coverslip.

Integrin staining. RBL-2H3 cells expressing GFP-actin were grown on 15 mm round glass coverslips and fixed with 2% paraformaldehyde for 20 minutes at room temperature. Cells were then permeabilised by 10 minute incubation in 1% Triton and stained with anti-VLA4 (anti-α4; Endogen, Boston, MA) or anti-β3 (H-96; Santa Cruz Biotchnology, Inc., Santa Cruz, CA) primary antibodies, followed by incubation with Alexa555-conjugated secondary antibodies (Alexa Fluor® 555 $F(ab')_2$ fragment of goat anti-mouse IgG (Invitrogen, Carlsbad, CA) for anti-VLA4 and Alexa Fluor® 555 donkey anti-rabbit IgG (Invitrogen, Carlsbad, CA) for anti-β3). Coverslips were then mounted in ProLong Gold® anti-fade reagent (Invitrogen, Carlsbad, CA) and imaged on a Zeiss LSM510 META confocal imaging system.

Gene constructs and transfection

The γ subunit of human FcεRI (Accession number NM 004106; GI 4758343) was initially cloned into the EcoRI/SalI site of pCMV6-XL5 (OriGene, Rockville, MD), followed by restriction digest-mediated transfer, in frame with mCFP, into pEF-DEST51 expression vector (Invitrogen, Carlsbad, CA). The pmaxGFP vector was supplied as part of the Cell Line Nucleofector Kit L (Amaxa, Gaithersburg, MD). Transfection was accomplished by introduction of the vector into early passage RBL-2H3 cells using the Amaxa Nucleofector II with Solution L and Program T-20 (Amaxa, Gaithersburg, MD). RBL-2H3 cells transiently transfected with pmaxGFP were imaged within 24 hours. Cells stably transfected with pEF-FcεRIγ-mCFP were selected with 2.5 μg/ml Blasticidin (Invitrogen, Carlsbad, CA), followed by fluorescence associated cell sorting (FACS) for CFP emission.

Image Registration

For two colour imaging, fluorescence was separated into two spectrally distinct images by a dual colour image splitter (OptoSplit II, Cairn Research, UK), which were captured simultaneously and side-by-side on a single CCD camera (iXon 897 or Luca, Andor UK). The spectral windows of the captured images were defined by a dichroic filter and two emission filters in the image splitter (565DXCR, D510/40m, D655/40m, respectively, Chroma, Rockingham, VT). The relative translation of one image with respect to the other on the CCD camera was calibrated by imaging multi–fluorophore fluorescent beads (0.2 μm Tetraspeck, Invitrogen, Carlsbad, CA) that have an emission spectrum covering the two spectral windows. The translation vector was found using an iterative cross-correlation routine providing sub-pixel accuracy[7]. The quality of the alignment (merging) of the two images was limited only by small aberrations present in one or both of the channels that lead to a typical 10 nm error towards the center of the image (where the alignment routine was biased) to a 30 nm error towards the edges of the images.

Image Processing

All data analysis and image processing was performed within the MATLAB (The Mathworks Inc.) environment, including the DIPImage[8] image processing library. Single particle tracking algorithms were coded in the c language and called from within MATLAB through a mex interface. For essential speed optimisation (~20 X speedup over a MATLAB implementation), the Richardson-Lucy deconvolution code was written using the CUDA toolkit[9] (NVIDIA, Santa Clara, CA) to allow calculation using a graphics processing unit (NVIDIA 8800 GTS), and was called from within the MATLAB environment through a mex interface. Confocal images were de-noised using a two dimensional wavelet based filter[5,10].

Single Particle Tracking

Single particle trajectories were determined from the raw data sets using a three step process: (1) identification of areas of interest; (2) Gaussian fitting; (3) building trajectories from coordinates. This approach is similar to those described previously[11-14].

1. Identification of areas of interest. Each 2D image from a 3D data set was processed independently to find QD coordinates. Areas of interest were contiguous regions of pixels that met two criteria: (a) pixels had intensities greater than three times the standard deviation of pixel intensities from areas defined as background (backgroundoffset algorithm, [8]) and (b) pixels were above a threshold, (threshold, [8]). Afterwards, a high pass filtering of the image was performed by subtracting from the image a 2D Gaussian filter with $\sigma = 5$. The result is a binary image of pixels that passed both criteria.

2. Gaussian fitting. The center of mass of each contiguous region in the binary image was used as a starting point in a Gaussian fitting routine. The raw 2D images were used being offset to zero. The highest intensity pixel in a small region around the starting point (typically 5 pixels square) was used as an updated starting point to the iterative "Gaussian mask"[15] fitting routine. Fits were performed in a square region, of size $\sim 2 \times \sigma_{psf}$, around the updated starting point, where σ_{psf} defines the size of 2D Gaussian approximation to the

point spread function. After convergence of the fitting routine, defined as a change in location of less than 10^{-5} pixels, a normalised cross-correlation was calculated using the data and a 2D Gaussian with center given by the result of the fit. The found coordinates were only considered as positions of QDs and used in further analysis if they exceeded a cross-correlation value of 0.7.

3. Building trajectories from coordinates. The probability of finding a diffusing particle in two dimensions at a distance greater than *r* from its starting point after a time Δt is given by[16]

$$P(r,\Delta t)=\exp[-r^2/(4D\Delta t)] \qquad \text{eq. 1}$$

Trajectories were built from the set of 3D coordinates in two steps. First, coordinates identified at time *t* were compared with coordinates at time $t+\Delta t$ using eq. 1 where Δt is the inverse frame rate of data acquisition. If $P(r,\Delta t)$ was found to be greater than .05, the coordinate at $t+\Delta t$ is associated with the coordinate at *t* in a trajectory. This process builds short, un-interrupted trajectories. Due to the blinking of QDs, temporally separated trajectories may correspond to the movement of the same QD. The end coordinate of all trajectories are compared with all later starting coordinates of other trajectories using eq. 1, where Δt is now the time interval between the end of the first trajectory and the beginning of the second. The later trajectory with the smallest Δt that has a $P(r,\Delta t)>.01$ is connected with the first trajectory. This process is continued until there are no remaining pairs of trajectories that satisfy the criteria. If a trajectory contains more than four coordinates, a diffusion coefficient is estimated from the trajectory as

$$D_{est}=MSD(\Delta t) / 4\Delta t \qquad \text{eq. 2.}$$

where *MSD* is the mean square displacement and Δt is the inverse frame rate. The diffusion coefficient, *D*, used in eq. 1 is then the mean diffusion coefficient from the two trajectories. If the diffusion coefficient of the two trajectories varies by more than a factor of ten, trajectories are not combined.

Short range interaction analyses

RBL-2H3 cells were labeled with 200 pM each QD655-IgE and QD585-IgE for 10 min at 37°C. TIRF imaging was performed on these cells at 100 frames/s at 35°C and the resulting QD-IgE-FcεRI time series were then tracked as described (see Supplementary Methods, Single Particle Tracking section) to generate sets of trajectories for each colour QD. All trajectories from one colour of QD were compared with all trajectories of the other colour. If QDs of different colour were within a cutoff distance (500 nm) in the same time frame, a set of parameters was calculated based on the found positions of the QDs in the next time frame. All calculated parameters were recorded as a function of initial separation. Uncorrelated jump distance and jump magnitude were calculated to determine if coordinated movement or transient dimerisation existed between the tracked QD-IgE-FcεRI complexes. These parameters were averaged over all frames and QD pairs into 50 nm separation bins and then plotted, with the error given as the standard error of the mean in each bin. The degree of correlation between the motions of two particles was obtained by determing the amount of uncorrelated motion between two nearby particles: $D_i = |\mathbf{J}_i - \mathbf{J}_i(\mathbf{J}_i \cdot \mathbf{J}_j)/(|\mathbf{J}_j||\mathbf{J}_i|)|$, where $\boldsymbol{J1}_i=\boldsymbol{r1}_{i+1}-\boldsymbol{r1}_i$, $\boldsymbol{J2}_i=\boldsymbol{r2}_{i+1}-\boldsymbol{r2}_i$, and $\boldsymbol{r}_i$ is the position of a particle in frame *i*. The magnitude of single time step displacements, $|\boldsymbol{J}_i|$, was calculated in a similar manner. Parameters without a particle index (1,2) are calculated for both QDs.

Deconvolution

Deconvolution of time series images involved several steps. First, the pixel regions in each three dimensional data stack that corresponded to actin regions were cropped to form smaller three dimensional data sets and filtered in the time dimension with a Gaussian filter with σ = 10 frames (0.3 seconds). For manageable processing of several hundred data sets, each data set containing 2,000 images, only 1 of 10 time filtered images were deconvolved, starting with frame 5 and ending with frame 1,995. These 200 images first had a pixel-wise camera offset subtracted from them and then were independently de-noised using a two dimensional wavelet based filter[5,10]. To prevent edge related artifacts during deconvolution, each image was mirrored along each edge by 16 pixels that were then multiplied by a cosine function that went to zero at the outermost pixel. A two dimensional Gaussian was used to represent the microscope point spread function (PSF). The width of the PSF was determined by a fit to a high signal to noise image of a 100 nm bead (Tetraspeck, Invitrogen, Carlsbad,

CA). Two hundred iterations of a Richardson-Lucy deconvolution[17,18] were performed on each image with an entropy regularisation[19] after each iteration with regularisation parameter of 0.05. After deconvolution, images were cropped to their original size.

Binary Segmentation of Actin Structures

The deconvolved time series images were used for actin segmentation. Each image was filtered, and segmented using a four step process. First, a top hat filter (DIPImage function 'tophat') selects regions that are above a local minimum. Second, the top hat filtered image is eroded using grey scale erosion (DIPImage 'erosion') to better define the brightest regions. Third, the image is locally contrast stretched by dividing each pixel by the maximum value found in a 10 pixel (0.67 micron) radius around each pixel. Finally, the resulting image is thresholded (DIPImage function 'threshold') to create a binary image representing the location of actin structures.

Actin Trajectory Overlap

Coordinates found from single particle tracking were used to build binary trajectory images that were compared with actin structures. If a coordinate was valid (QD has not 'blinked' off) in both a time frame t and the next time frame at t+1, a binary image was created of this single time frame jump by drawing a pixelised line from the starting point to the end point. The linear pixel size used is the back-projected pixel size of the collected CCD images, which was 67 nm. For all valid single frame jumps in each trajectory found by single particle tracking, the total length of the linearised trajectory, as well as the number of pixels in the trajectory that overlapped with the binary actin image at time t were recorded. For each trajectory, the same calculation was made using 10 simulated particles that had the same starting coordinate, diffusion coefficient, trajectory length, and blinking behaviour as that of the single particle trajectory, but were otherwise unrestricted.

To test if the found trajectories had behaviour with respect to actin that was significantly different from the unrestricted, simulated particles with the same diffusion coefficient, we treated the system using a binomial model as follows. Within groupings for each cell treatment, all trajectories were combined to give a total trajectory length n, and a total actin overlap k. The simulated particle trajectories were used to define a probability for overlap p for the unrestricted case. We make the simplification that all pixels in a trajectory can be treated independently with respect to actin overlap in order to use the well defined binomial model. The cumulative distribution function of the binomial distribution is $F(k;n,p)=I_{1-p}(n-k,k+1)$ where I is the regularised incomplete beta function. F gives the probability that a randomly generated data set created from the binomial model with parameters n and p would have a value less than or equal to k. We reject the hypothesis that our trajectories can be modeled with unrestricted diffusion with respect to actin when F is less than .01. In all three cases, $F<<<0.01$, with $F = 2.35\text{x}10^{-286}$, $2.35\text{x}10^{-264}$ and $2.42\text{x}10^{-154}$ in the resting, latrunculin-treated, and PMA-treated cells, respectively.

Diffusion in proximity to actin

A pixelated distance map to the nearest actin structure was found by a distance transform (DIPImage function 'dt') of the inverse of the binary images created by the binary segmentation of the actin images. The mean square jump distance of single time step jumps was recorded as function of distance from actin for all SPT trajectories in cells treated with PMA.

An offset term was calculated by fitting individual particle trajectories to Eq.(1) using the first 3 data points of the MSD. This value is equivalent to the first point of a calculated MSD plot and can be related to the diffusion coefficient.

The mean observed jump size over some time interval of a freely diffusing particle (and thereby calculated diffusion coefficient) will appear to be reduced near a reflecting boundary due to the particle's inability to make large jumps in the direction of the boundary [20]. In order to estimate the magnitude of this effect, simulations of a diffusing particle near a reflecting half space boundary were performed using the pixel size and frame rate of the experiment with parameters that correspond to the median experimentally observed $D_{1\text{-}3}$ diffusion coefficient found as described above. To represent detector time averaging, 10 sub-frames at 10 times the frame rate were

added together to form one simulated observed frame. If a particle's position after a jump in one of the sub-frames was beyond the reflecting boundary (x = 0), its x-coordinate was multiplied by -1 and the next frame was calculated as a jump from the corrected position. The resulting time series were analysed with the same routines used for experimental data.

Supplementary References

1. Destainville, N. & Salome, L. Quantification and correction of systematic errors due to detector time-averaging in single-molecule tracking experiments. *Biophysical Journal* **90**, L17-L19 (2006).
2. Kusumi, A., Sako, Y. & Yamamoto, M. Confined Lateral Diffusion of Membrane-Receptors as Studied by Single-Particle Tracking (Nanovid Microscopy) - Effects of Calcium-Induced Differentiation in Cultured Epithelial-Cells. *Biophysical Journal* **65**, 2021-2040 (1993).
3. Pfeiffer, J. R. & Oliver, J. M. Tyrosine Kinase-Dependent Assembly of Actin Plaques Linking Fc-Epsilon-R1 Cross-Linking to Increased Cell Substrate Adhesion in Rbl-2h3 Tumor Mast-Cells. *Journal of Immunology* **152**, 270-279 (1994).
4. Wilson, B. S., Pfeiffer, J. R., Surviladze, Z., Gaudet, E. A. & Oliver, J. M. High resolution mapping of mast cell membranes reveals primary and secondary domains of Fc epsilon RI and LAT. *Journal of Cell Biology* **154**, 645-658 (2001).
5. Rooms, F., Philips, W. & Lidke, D. S. Simultaneous degradation estimation and restoration of confocal images and performance evaluation by colocalization analysis. *Journal of Microscopy-Oxford* **218**, 22-36 (2005).
6. Pfeiffer, J. R., Seagrave, J. C., Davis, B. H., Deanin, G. G. & Oliver, J. M. Membrane and Cytoskeletal Changes Associated with Ige-Mediated Serotonin Release from Rat Basophilic Leukemia-Cells. *Journal of Cell Biology* **101**, 2145-2155 (1985).
7. Pham, T. Q., Bezuijen, M., van Vliet, L. J., Schutte, K. & Hendriks, C. L. L. Performance of optimal registration estimators. *Proceedings of the SPIE - The International Society for Optical Engineering* **5817**, 133-144 (2005).
8. Luengo Hendriks, C. L., Rieger, B., van Ginkel, M., van Kempen, G. M. P. & van Vliet, L. J. "DIPimage: A scientific image processing toolbox for MATLAB" Delft Univ. Technol., Delft, The Netherlands. Available: http://www.qi.tnw.tudelft.nl/DIPlib (1999).
9. NVIDIA. Compute Unified Device Architecture (CUDA). http://developer.nvidia.com/object/cuda.html (2007).
10. Sendur, L. & Selesnick, I. W. Bivariate shrinkage functions for wavelet-based denoising exploiting interscale dependency. *Ieee Transactions on Signal Processing* **50**, 2744-2756 (2002).
11. Arndt-Jovin, D. J. *et al.* In vivo cell imaging with semiconductor quantum dots and noble-metal nanodots. *Proc. of SPIE* **6096**, 1-10 (2006).
12. Bonneau, S., Dahan, M. & Cohen, L. D. Single quantum dot tracking based on perceptual grouping using minimal paths in a spatiotemporal volume. *Ieee Transactions on Image Processing* **14**, 1384-1395 (2005).
13. Dahan, M. *et al.* Diffusion dynamics of glycine receptors revealed by single-quantum dot tracking. *Science* **302**, 442-445 (2003).
14. Hagen, G. M. *et al.* in Single Molecule Dynamics (Wiley Press, In Press).
15. Thompson, R. E., Larson, D. R. & Webb, W. W. Precise nanometer localization analysis for individual fluorescent probes. *Biophysical Journal* **82**, 2775-2783 (2002).
16. Saxton, M. J. Lateral Diffusion in an Archipelago - Single-Particle Diffusion. *Biophysical Journal* **64**, 1766-1780 (1993).
17. Lucy, L. B. Iterative Technique for Rectification of Observed Distributions. *Astronomical Journal* **79**, 745-754 (1974).
18. Richards.Wh. Bayesian-Based Iterative Method of Image Restoration. *Journal of the Optical Society of America* **62**, 55-& (1972).

19. de Monvel, J. B., Le Calvez, S. & Ulfendahl, M. Image restoration for confocal microscopy: Improving the limits of deconvolution, with application to the visualization of the mammalian hearing organ. *Biophysical Journal* **80**, 2455-2470 (2001).
20. Ritchie, K. *et al.* Detection of non-Brownian diffusion in the cell membrane in single molecule tracking. *Biophys J* **88**, 2266-77 (2005).